LAPAR: Linearly-Assembled Pixel-Adaptive Regression Network for Single Image Super-Resolution and Beyond

Wenbo Li[1]* **Kun Zhou**[2]* **Lu Qi**[1] **Nianjuan Jiang**[2] **Jiangbo Lu**[2]† **Jiaya Jia**[1,2]
[1]The Chinese University of Hong Kong [2]Smartmore Technology
`{wenboli,luqi,leojia}@cse.cuhk.edu.hk`
`{kun.zhou,nianjuan.jiang,jiangbo}@smartmore.com`

Abstract

Single image super-resolution (SISR) deals with a fundamental problem of upsampling a low-resolution (LR) image to its high-resolution (HR) version. Last few years have witnessed impressive progress propelled by deep learning methods. However, one critical challenge faced by existing methods is to strike a sweet spot of deep model complexity and resulting SISR quality. This paper addresses this pain point by proposing a linearly-assembled pixel-adaptive regression network (LAPAR), which casts the direct LR to HR mapping learning into a linear coefficient regression task over a dictionary of multiple predefined filter bases. Such a parametric representation renders our model highly lightweight and easy to optimize while achieving state-of-the-art results on SISR benchmarks. Moreover, based on the same idea, LAPAR is extended to tackle other restoration tasks, e.g., image denoising and JPEG image deblocking, and again, yields strong performance.

1 Introduction

Single image super-resolution aims at reconstructing a high-resolution (HR) image from a low-resolution (LR) one. Due to its wide applications, intensive research efforts and great progress have been made in the past decades. Among existing methods, the simplest one is to adopt basic spatially invariant nearest-neighbor, bilinear and bicubic interpolation. However, these simple linear methods neglect the content variety of natural images, and usually overly smooth the structures and details.

To better adapt to different image elements, sparse dictionary learning processes pixels (or patches) individually. Early work [1, 2, 3, 4] learned a pair of dictionaries of LR and HR patches where sparse coding is shared in the LR and HR space. During inference, given trained dictionaries, only sparse coding is optimized to complete estimation. Dictionary-based methods generally yield stable results. However, the difficulty of joint optimization in the training process still affects recovery performance. Taking an example-based learning approach, Romano *et al*. [5] hashed image patches into clusters based on local gradient statistics, and a single filter is constructed and applied per cluster. Despite simple, such a hard-selection operation is discontinuous and non-differential. Meanwhile, it only provides compromised rather than optimal solutions for varying input patterns.

Recently, a great number of deep learning methods [6, 7, 8, 9, 10, 11, 12, 13, 14, 15, 16] were proposed to predict the LR-HR mapping. The challenge lies in the unconstrained nature of image contents [17], where training can be unstable when largely varying stochastic gradients exist. It causes annoying artifacts. Residual learning, attention mechanism and other strategies were used to alleviate these issues. Also, this line of methods is highly demanding on computational resources.

*Equal contribution
†Corresponding author

34th Conference on Neural Information Processing Systems (NeurIPS 2020), Vancouver, Canada.

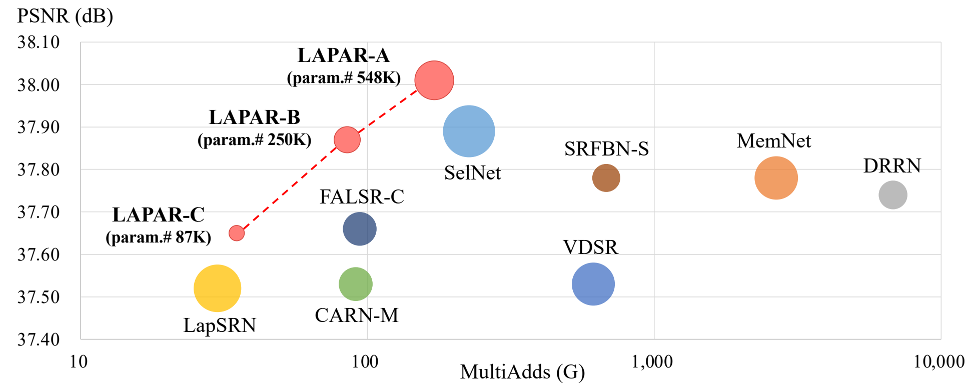

Figure 1: Comparison between our proposed LAPAR and other lightweight methods ($<$ 1M parameters) on Set5 [27] for $\times 2$ setting. Circle sizes are set proportional to the numbers of parameters.

Different from the straightforward estimation, adaptive filters (kernels) can group neighboring pixels in a spatially variant way. It has been proven effective in tasks of super-resolution [18, 19, 20], denoising [17, 21], video interpolation [22] and video prediction [23, 24, 25]. The benefits brought in are twofold. First, the estimated pixels always lie within the convex hull of surroundings to avoid visual artifacts. Second, the network only needs to evaluate the relative importance of neighbors rather than predicting absolute values, which speeds up the learning process [26, 17]. Nevertheless, many methods estimate filters without regularization terms, which are useful to constrain the solution space of the ill-posed SISR problem.

In this paper, we tackle the efficient learning and reconstruction problem of SISR by utilizing a linear space constraint, and propose a linearly-assembled pixel-adaptive regression network (LAPAR). The core idea is to regress and apply pixel-adaptive “enhancement" filters to a cheaply interpolated image (by bicubic upsampling). Specifically, we design a lightweight convolutional neural network to learn linear combination coefficients of predefined filter bases for every input pixel. Despite spatially variant, the estimated filters always lie within a linear space assembled from atomic filters in our dictionary, and are easy and fast to optimize. In combination with the LAPAR network to achieve state-of-the-art SISR results, our dictionary of filter bases can be surprisingly common and simple, which are basically dozens of (anisotropic) Gaussian and difference of Gaussians (DoG) kernels.

The overall contributions of this paper are threefold:

- We propose LAPAR for SISR. Figure 1 shows that LAPAR achieves state-of-the-art results with the least model parameters and MultiAdds among all existing lightweight networks.
- Different from previous methods, we predefine a set of meaningful filter bases and turn to optimize assembly coefficients in a pixel-wise manner. Extensive experiments demonstrate the advantages of this learning strategy, as well as its strength in accuracy and scalability.
- Based on the same framework, LAPAR can also be easily tailored to other image restoration tasks, e.g., image denoising and JPEG image deblocking, and yields strong performance.

2 Method

Before presenting the LAPAR approach, we first give a brief revisit to image super-resolution.

2.1 Revisiting Image Super-Resolution

In the single image super-resolution (SISR) task, for a high-resolution (HR) vectorized image $\mathbf{y} \in \mathbb{R}^{HWs^2}$, the low-resolution (LR) courterpart $\mathbf{x} \in \mathbb{R}^{HW}$ is generally formulated as

$$\mathbf{x} = \mathbf{SHy}\,, \tag{1}$$

where $\mathbf{H} \in \mathbb{R}^{HWs^2 \times HWs^2}$ is a blurring filter and $\mathbf{S} \in \mathbb{R}^{HW \times HWs^2}$ represents the downsampling operator. The goal of SISR is to recover $\mathbf{y}$ from the given LR image $\mathbf{x}$. However, it is clear that

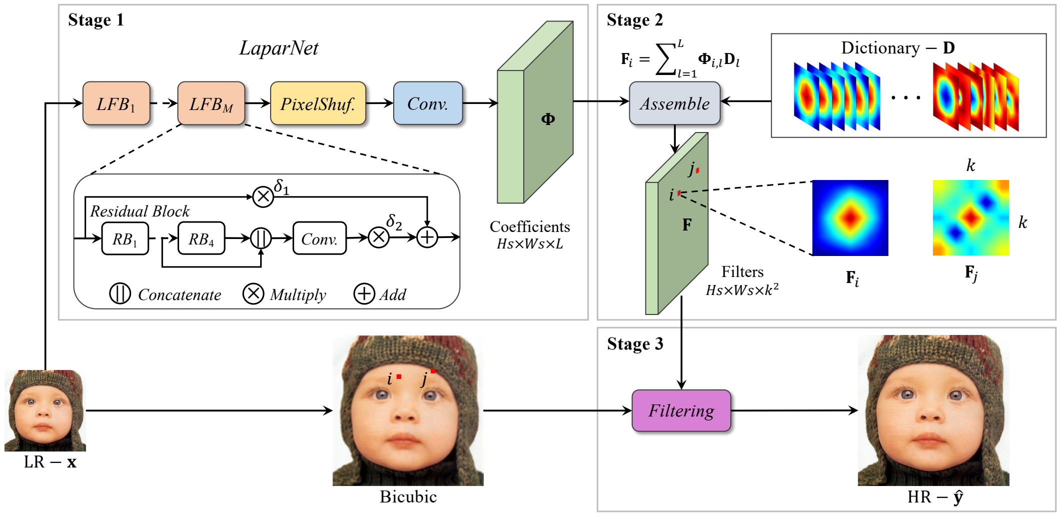

Figure 2: Framework of linearly-assembled pixel-adaptive regression network (LAPAR). Our method consists of three primary stages, i.e., stage 1: regressing linear combination coefficients; stage 2: assembling pixel-adaptive filters; stage 3: applying adaptive filters to the bicubic upsampled image.

SISR is an ill-posed problem since infinite possible solutions of $\mathbf{y}$ can be derived. Apart from the reconstruction constraints, more image priors or constraints are required to tackle this problem.

2.2 Our Learning Strategy

Instead of estimating the LR-HR mapping, we learn the correspondence between the cheaply interpolated (e.g., by bicubic upsampling) image and HR to construct our fast and robust solution.

In the first step, we extend the cheaply upsampled result to $\mathbf{B} \in \mathbb{R}^{HWs^2 \times k^2}$, a matrix consisting of HWs^2 patches with size k^2 ($k = 5$ in this paper). The i-th target pixel $\mathbf{y}_i$ is predicted by integrating neighboring pixels $\mathbf{B}_i$ (the i-th row of $\mathbf{B}$) centered at the coordinate of $\mathbf{y}_i$. The objective function is formulated as

$$\min_{\mathbf{F}_i} \|\mathbf{F}_i {\mathbf{B}_i}^T - \mathbf{y}_i\|_2^2 \,, \tag{2}$$

where $\mathbf{F} \in \mathbb{R}^{HWs^2 \times k^2}$ is the filter matrix that needs to be estimated. In our method, filters are learned in a spatially variant way for rich visual details.

To deal with ill-posed problems, previous works have adopted different regularization terms, such as l_1-norm [1, 2, 3, 4], l_2-norm [28], total variation (TV) [29, 30] and anisotropic diffusion [31]. With the regularization term, the optimization objective of $\mathbf{F}_i$ is defined as follows,

$$\min_{\mathbf{F}_i} \|\mathbf{F}_i {\mathbf{B}_i}^T - \mathbf{y}_i\|_2^2 + \lambda R\left(\mathbf{F}_i\right), \tag{3}$$

where λ is a balancing parameter and R is the regularization function. It is nontrivial to determine unifying regularization that can be optimized efficiently and is also general enough for different tasks. Thus, instead of designing a hand-crafted term, we introduce a linear space constraint to facilitate the optimization, which is analogous to the idea of the popular parametric human body space (e.g., SMPL [32]) in spirit. Specifically, a filter $\mathbf{F}_i$ in our method is represented as a linear combination of a set of underlying base filters:

$$\mathbf{F}_i = \mathbf{\Phi}_i \mathbf{D} \,, \tag{4}$$

where $\mathbf{D} \in \mathbb{R}^{L \times k^2}$ represents a dictionary consisting of L filter bases, and $\mathbf{\Phi} \in \mathbb{R}^{HWs^2 \times L}$ refers to the linear combination coefficients. Unlike traditional dictionary learning methods [1, 2, 3, 4] that optimize $\mathbf{D}$ and $\mathbf{\Phi}$ simultaneously, we simplify the learning procedure and only optimize coefficients $\mathbf{\Phi}$ by predefining a meaningful dictionary as detailed in Sect. 2.3. It is clear that the proposed strategy is well-conditioned as long as the dictionary $\mathbf{D}$ is over-complete and can well represent the desired k^2-sized filters for different pixels. Now, optimization of $\mathbf{F}_i$ becomes optimizing $\mathbf{\Phi}_i$ equivalently:

$$\min_{\mathbf{\Phi}_i} \|\mathbf{\Phi}_i \mathbf{D} {\mathbf{B}_i}^T - \mathbf{y}_i\|_2^2 \,. \tag{5}$$

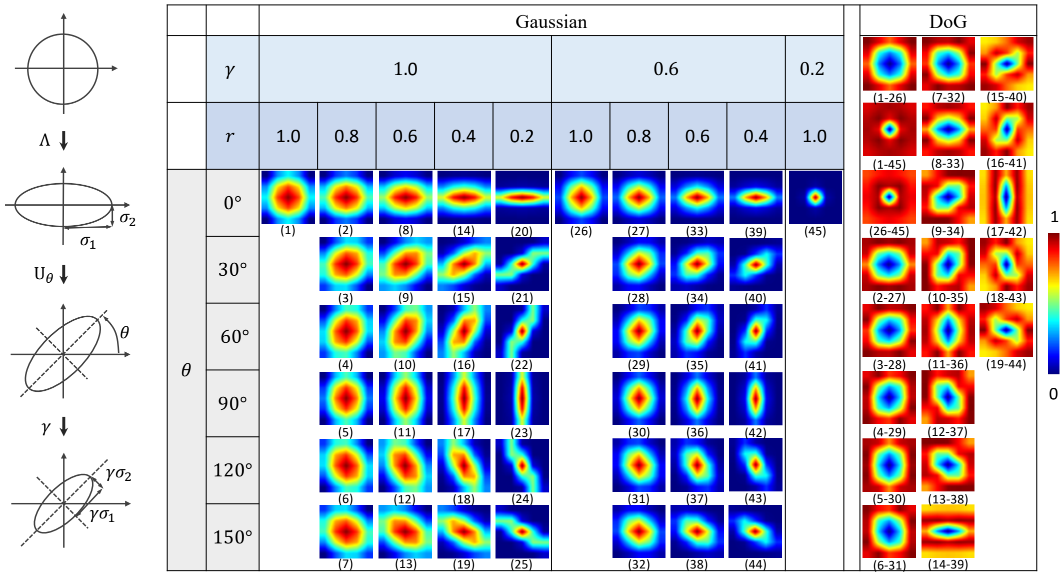

Figure 3: Visualization of part of the filters in the proposed dictionary. Symbols γ, θ, r describe scaling, rotation and elongation ratio ($r = \sigma_2/\sigma_1$). The Gaussian is denoted by (a), and DoG (a-b) means the difference of Gaussian (a) and Gaussian (b). When $\gamma = 1$ and $r = 0.2$, there is a Gaussian every 15° (six of them omitted from display). For better visualization, filters are normalized to $[0, 1]$.

We propose a convolutional network (i.e., $LaparNet$) as shown in Figure 2 to estimate the coefficient matrix $\mathbf{\Phi} = LaparNet(\mathbf{x})$. The network details will be presented in Sect. 2.4. Based on the regressed linear coefficients $\mathbf{\Phi}_i$ for the i-th pixel, its high-resolution prediction $\hat{\mathbf{y}}_i$ is derived as

$$\hat{\mathbf{y}}_i = \mathbf{\Phi}_i \mathbf{D} \mathbf{B}_i{}^T . \tag{6}$$

In the training process, we use the Charbonnier loss as the error metric, which takes the form of

$$Loss = \sqrt{\|\hat{\mathbf{y}} - \mathbf{y}\|_2^2 + \epsilon^2} , \tag{7}$$

where ϵ is a small constant. The parameters of the network are optimized by gradient descent. Without the bells and whistles, our proposed method obtains decent performance as illustrated in Sect. 3.

2.3 Dictionary Design

In this paper, we provide a redundant dictionary with 72 underlying filters (with $L > k^2$, implying that it is redundant). The dictionary is merely composed of Gaussian and difference of Gaussians (DoG) filters mainly for two reasons. First, as discussed in [33, 34, 35], Gaussians have strong representation ability. Second, difference of Gaussians has been verified to increase the visibility of edges and details [36, 37, 38, 39].

The corresponding elliptical function of Gaussian has the form as

$$G\left(\mathbf{x} - \mathbf{x}'; \mathbf{\Sigma}\right) = \frac{1}{2\pi |\mathbf{\Sigma}|^{\frac{1}{2}}} \exp\{-\frac{1}{2}\left(\mathbf{x} - \mathbf{x}'\right)^T \mathbf{\Sigma}^{-1} \left(\mathbf{x} - \mathbf{x}'\right)\} , \tag{8}$$

where $\mathbf{x}$ and $\mathbf{x}'$ are coordinates of neighboring pixels and central pixel respectively, and the covariance matrix $\mathbf{\Sigma}$ can be decomposed into

$$\begin{aligned} \mathbf{\Sigma} &= \gamma^2 \mathbf{U}_\theta \mathbf{\Lambda} \mathbf{U}_\theta{}^T , \\ \mathbf{U}_\theta &= \begin{bmatrix} \cos\theta & -\sin\theta \\ \sin\theta & \cos\theta \end{bmatrix} , \\ \mathbf{\Lambda} &= \begin{bmatrix} \sigma_1^2 & 0 \\ 0 & \sigma_2^2 \end{bmatrix} , \end{aligned} \tag{9}$$

where $\gamma, \theta, \sigma_{1/2}$ are scaling, rotation and elongation parameters. The decomposition of Eq. (9) is schematically explained in the left-hand side of Figure 3. Inspired by [5, 40] that train filters based on local structure statistics, we define the Gaussians with different parameter settings as shown in Figure 3. In general, a Gaussian with a large disparity of σ_1 and σ_2 is supposed to preserve edges well. Based on the anisotropic Gaussian kernels in our dictionary, we generate DoG filters as follows,

$$DoG\left(\mathbf{x}-\mathbf{x}';\mathbf{\Sigma}_1,\mathbf{\Sigma}_2\right)=G\left(\mathbf{x}-\mathbf{x}';\mathbf{\Sigma}_1\right)-G\left(\mathbf{x}-\mathbf{x}';\mathbf{\Sigma}_2\right)\ , \tag{10}$$

which allows negative values. All 72 filters are normalized to sum total to 1.

2.4 Network Architecture

We adopt a lightweight residual network to predict combination coefficients of filters. It consists of multiple local fusion blocks (LFB) [41], a depth-to-space (PixelShuffle) layer and several convolutional layers in the tail. The depth-to-space layer is used to map LR features to HR ones, and the final convolutional layers generate combination coefficients. Besides, weight normalization [26] is employed to accelerate the training process. To evaluate the network scalability, we provide three models according to the number of feature channels (C) and local fusion modules (M), and name them as LAPAR-A (C32-M4), LAPAR-B (C24-M3), and LAPAR-C (C16-M2) (see also Figure 1).

3 Experiments

3.1 Datasets and Metrics

In our experiments, the network is trained with DIV2K [42] and Flickr2K image datasets. During the testing stage, based on the peak signal to noise ratio (PSNR) and the structural similarity index (SSIM) [43], multiple standard benchmarks including Set5 [27], Set14 [2], B100 [44], Urban100 [45], Manga109 [46] are used to evaluate the performance of our method. Following previous methods [47, 19, 15], only results of the Y channel from the YCbCr color space are reported in this paper.

3.2 Training Details

We use eight NVIDIA GeForce RTX 2080Ti GPUs to train the network with a mini-batch size of 32 for 600K iterations. The optimizer is Adam. We adopt a cosine learning rate strategy with an initial value of $4e-4$. The input patch size is set to 64×64. Data augmentation is performed with random cropping, flipping and rotation. The flipping involves vertical or horizontal versions, and the rotation angle is $90°$.

3.3 Study of The Filter Dictionary

In this section, we evaluate how the dictionary design affects the final result and also the optimization of the proposed learning strategy.

Type	Num.	Set5	B100
G + DoG	72	**38.01**	**32.19**
Learned	72	37.98	**32.19**
RAISR [5]	72	37.93	32.12
Random	72	37.88	32.08
G + DoG	24	37.94	32.13
G + DoG	14	37.87	32.07
Random	14	37.80	32.01

Table 1: PSNR(dB) results of different dictionary settings for LAPAR-A on $\times2$ scale on Set5 and B100.

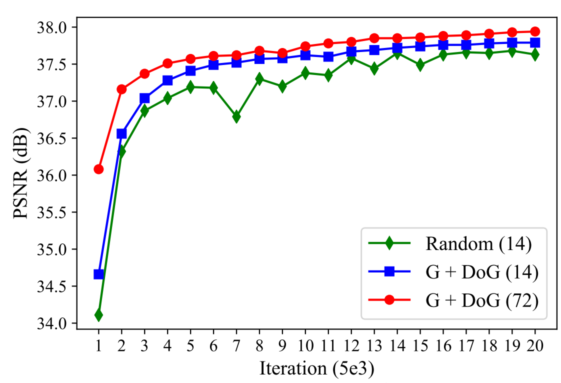

Figure 4: Validation results on Set5 during training.

As aforementioned, we adopt a dictionary composed of 72 Gaussian and DoG filters to capture more structural details. To verify whether the proposed filters are effective or not, we conduct additional experiments by replacing them with random filters or RAISR [5] filters or filters directly learned

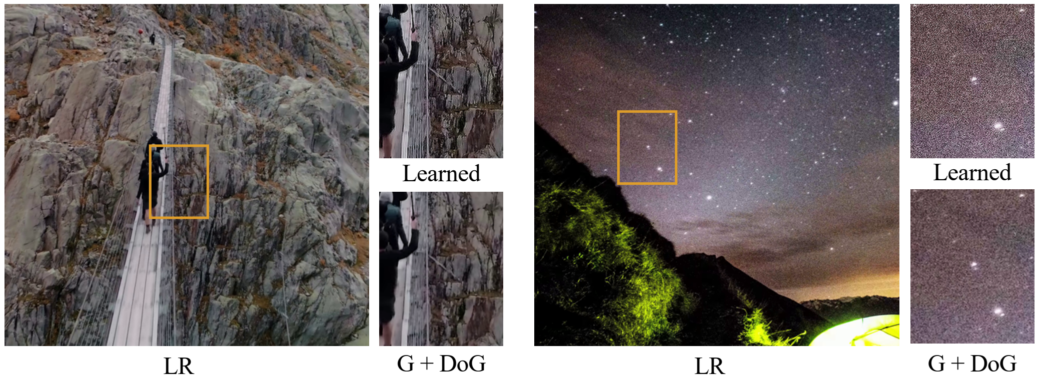

Figure 5: Visualization of the super-resolved images ($\times 2$) generated by learned filters as well as Gaussian and DoG filters. Zoom in for better visual comparison.

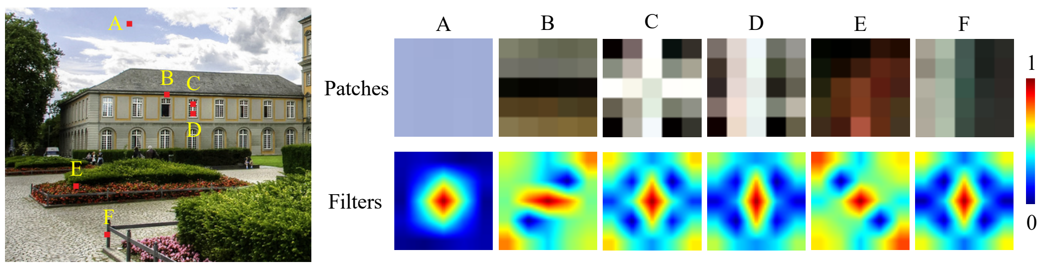

Figure 6: Visualization of the final assembled filters of LAPAR for different pixel locations.

by networks. For fairness, the size of filters learned from RAISR is also set to 5×5 (contrary to original 11×11). As reported in Table 1, it is clear that our proposed Gaussian and DoG combination achieves the best result. Although the learned filters obtain comparable results, we find they may sometimes generate artifacts along edges or amplify noise due to overfitting in natural images, as shown in Figure 5. Interestingly, random filters can still achieve competitive performance, which further manifests the feasibility of our proposed learning strategy with the provided dictionary.

We also explore the influence caused by the number of filters on LAPAR-A. Table 1 shows that the dictionary with 72 basic filters yields a better result than the 24 and 14 versions. This study indicates a sufficiently large dictionary with diverse filters is indeed helpful to obtain superior results.

Experiments have also verified that our proposed model enables fast optimization. Figure 4 illustrates the validation results on the Set5 benchmark during training. It is clear that our method reaches a decent level of reconstruction accuracy (e.g., over 37.5dB) after only a small number of iterations. In addition, compared with random filters, the Gaussian and DoG setting is more stable and accurate.

Finally, we visualize some examples of the final assembled filters in Figure 6. By estimating the spatially variant combination coefficients, our model generates adaptive filters to process the structural information differently for each pixel location. In flat areas, such as location A, the kernel tends to be isotropic. For horizontal (B), vertical (D, F) and diagonal (E) edges, one can see that the kernels are well constructed with corresponding orientations. The kernel of the cross-shaped pattern C is similar as D and F, but the weights are more evenly distributed.

3.4 Comparison with the State-of-the-Art Methods

To evaluate the performance of our approach, we make a comparison with state-of-the-art lightweight frameworks and show results in Table 2. For the $\times 2$ setting, LAPAR-A outperforms the other methods by a large margin on all benchmark datasets with even fewer parameters and MultiAdds. As the capacity of the network decreases, LAPAR-B and LAPAR-C still obtain competitive results gracefully (see also Figure 1). Even with only 80K parameters, the performance of LAPAR-C is superior to many existing methods. Regarding the $\times 3$ and $\times 4$ setting, our LAPAR-A again stands out as the best.

Scale	Method	Params	MultiAdds	Set5	Set14	B100	Urban100	Manga109
×2	SRCNN [6]	57K	53G	36.66/0.9542	32.42/0.9063	31.36/0.8879	29.50/0.8946	35.74/0.9661
	FSRCNN [53]	12K	6G	37.00/0.9558	32.63/0.9088	31.53/0.8920	29.88/0.9020	36.67/0.9694
	VDSR [7]	665K	613G	37.53/0.9587	33.03/0.9124	31.90/0.8960	30.76/0.9140	37.22/0.9729
	DRCN [9]	1,774K	17,974G	37.63/0.9588	33.04/0.9118	31.85/0.8942	30.75/0.9133	37.63/0.9723
	MemNet [54]	677K	2,662G	37.78/0.9597	33.28/0.9142	32.08/0.8978	31.31/0.9195	-
	DRRN [11]	297K	6,797G	37.74/0.9591	33.23/0.9136	32.05/0.8973	31.23/0.9188	37.92/0.9760
	LapSRN [10]	813K	30G	37.52/0.9590	33.08/0.9130	31.80/0.8950	30.41/0.9100	37.27/0.9740
	SelNet [55]	974K	226G	37.89/0.9598	33.61/0.9160	32.08/0.8984	-	-
	CARN-M [48]	412K	91G	37.53/0.9583	33.26/0.9141	31.92/0.8960	31.23/0.9193	-
	CARN [48]	1,592K	223G	37.76/0.9590	33.52/0.9166	32.09/0.8978	31.92/0.9256	-
	FALSR-B [56]	326k	75G	37.61/0.9585	33.29/0.9143	31.97/0.8967	31.28/0.9191	-
	FALSR-C [56]	408k	94G	37.66/0.9586	33.26/0.9140	31.96/0.8965	31.24/0.9187	-
	FALSR-A [56]	1,021K	235G	37.82/0.9595	33.55/0.9168	32.12/0.8987	31.93/0.9256	-
	SRMDNF [14]	1,513K	348G	37.79/0.9600	33.32/0.9150	32.05/0.8980	31.33/0.9200	-
	SRFBN-S [47]	282K	680G	37.78/0.9597	33.35/0.9156	32.00/0.8970	31.41/0.9207	38.06/0.9757
	LAPAR-C(Ours)	**87K**	**35G**	**37.65/0.9593**	**33.20/0.9141**	**31.95/0.8969**	**31.10/0.9178**	**37.75/0.9752**
	LAPAR-B(Ours)	**250K**	**85G**	**37.87/0.9600**	**33.39/0.9162**	**32.10/0.8987**	**31.62/0.9235**	**38.27/0.9764**
	LAPAR-A(Ours)	**548K**	**171G**	**38.01/0.9605**	**33.62/0.9183**	**32.19/0.8999**	**32.10/0.9283**	**38.67/0.9772**
×3	SRCNN [6]	57K	53G	32.75/0.9090	29.28/0.8209	28.41/0.7863	26.24/0.7989	30.59/0.9107
	FSRCNN [53]	12K	5G	33.16/0.9140	29.43/0.8242	28.53/0.7910	26.43/0.8080	30.98/0.9212
	VDSR [7]	665K	613G	33.66/0.9213	29.77/0.8314	28.82/0.7976	27.14/0.8279	32.01/0.9310
	DRCN [9]	1,774K	17,974G	33.82/0.9226	29.76/0.8311	28.80/0.7963	27.15/0.8276	32.31/0.9328
	MemNet [54]	677K	2,662G	34.09/0.9248	30.00/0.8350	28.96/0.8001	27.56/0.8376	-
	DRRN [11]	297K	6,797G	34.03/0.9244	29.96/0.8349	28.95/0.8004	27.53/0.8378	32.74/0.9390
	SelNet [55]	1,159K	120G	34.27/0.9257	30.30/0.8399	28.97/0.8025	-	-
	CARN-M [48]	412K	46G	33.99/0.9236	30.08/0.8367	28.91/0.8000	27.55/0.8385	-
	CARN [48]	1,592K	119G	34.29/0.9255	30.29/0.8407	29.06/0.8034	28.06/0.8493	-
	SRMDNF [14]	1,530K	156G	34.12/0.9250	30.04/0.8370	28.97/0.8030	27.57/0.8400	-
	SRFBN-S [47]	376K	832G	34.20/0.9255	30.10/0.8372	28.96/0.8010	27.66/0.8415	33.02/0.9404
	LAPAR-C(Ours)	**99K**	**28G**	**33.91/0.9235**	**30.02/0.8358**	**28.90/0.7998**	**27.42/0.8355**	**32.54/0.9373**
	LAPAR-B(Ours)	**276K**	**61G**	**34.20/0.9256**	**30.17/0.8387**	**29.03/0.8032**	**27.85/0.8459**	**33.15/0.9417**
	LAPAR-A(Ours)	**594K**	**114G**	**34.36/0.9267**	**30.34/0.8421**	**29.11/0.8054**	**28.15/0.8523**	**33.51/0.9441**
×4	SRCNN [6]	57K	53G	30.48/0.8628	27.49/0.7503	26.90/0.7101	24.52/0.7221	27.66/0.8505
	FSRCNN [53]	12K	5G	30.71/0.8657	27.59/0.7535	26.98/0.7150	24.62/0.7280	27.90/0.8517
	VDSR [7]	665K	613G	31.35/0.8838	28.01/0.7674	27.29/0.7251	25.18/0.7524	28.83/0.8809
	DRCN [9]	1,774K	17,974G	31.53/0.8854	28.02/0.7670	27.23/0.7233	25.14/0.7510	28.98/0.8816
	MemNet [54]	677K	2,662G	31.74/0.8893	28.26/0.7723	27.40/0.7281	25.50/0.7630	-
	DRRN [11]	297K	6,797G	31.68/0.8888	28.21/0.7720	27.38/0.7284	25.44/0.7638	29.46/0.8960
	LapSRN [10]	813K	149G	31.54/0.8850	28.19/0.7720	27.32/0.7280	25.21/0.7560	29.09/0.8845
	SelNet [55]	1,417K	83G	32.00/0.8931	28.49/0.7783	27.44/0.7325	-	-
	SRDenseNet [57]	2,015K	390G	32.02/0.8934	28.50/0.7782	27.53/0.7337	26.05/0.7819	-
	CARN-M [48]	412K	33G	31.92/0.8903	28.42/0.7762	27.44/0.7304	25.62/0.7694	-
	CARN [48]	1,592K	91G	32.13/0.8937	28.60/0.7806	27.58/0.7349	26.07/0.7837	-
	SRMDNF [14]	1,555K	89G	31.96/0.8930	28.35/0.7770	27.49/0.7340	25.68/0.7730	-
	SRFBN-S [47]	483K	1,037G	31.98/0.8923	28.45/0.7779	27.44/0.7313	25.71/0.7719	29.91/0.9008
	LAPAR-C(Ours)	**115K**	**25G**	**31.72/0.8884**	**28.31/0.7740**	**27.40/0.7292**	**25.49/0.7651**	**29.50/0.8951**
	LAPAR-B(Ours)	**313K**	**53G**	**31.94/0.8917**	**28.46/0.7784**	**27.52/0.7335**	**25.85/0.7772**	**30.03/0.9025**
	LAPAR-A(Ours)	**659K**	**94G**	**32.15/0.8944**	**28.61/0.7818**	**27.61/0.7366**	**26.14/0.7871**	**30.42/0.9074**

Table 2: Comparisons on multiple benchmark datasets for lightweight networks. The MultiAdds is calculated corresponding to a 1280 × 720 HR image. **Bold**/red/blue: **our**/best/second best results.

Although CARN [48] obtains comparable PSNR results, our method requires fewer parameters and performs better on SSIM. It further verifies that our method can lead to higher structural similarity. Meanwhile, compared with large EDSR [49], RCAN [50] and ESRGAN [51] and ProSR [52] that have parameters/PSNR as 43M/27.71dB, 16M/27.77dB, 17M/27.76dB and 16M/27.79dB under ×4 setting on the B100 dataset, our LAPAR-A model (0.66M/27.61dB) is **25**× – **65**× smaller, yet achieving quite similar super-resolution results. All these results justify the effectiveness of our method.

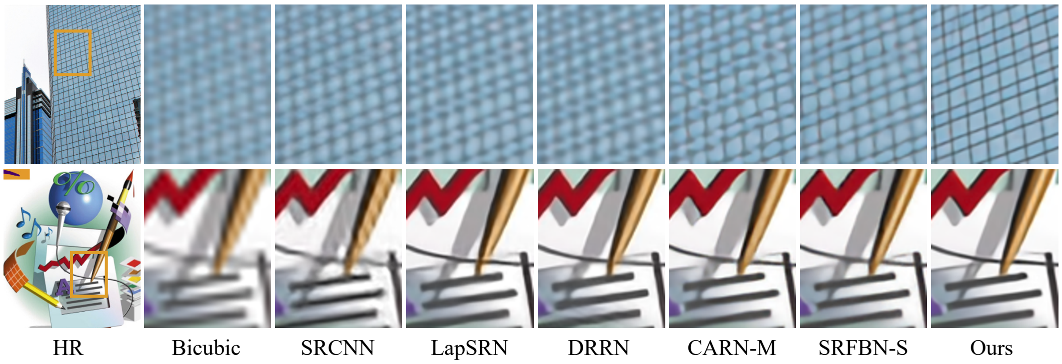

Figure 7: Image super-resolution examples on $\times 4$ scale of Urban100 and Set14.

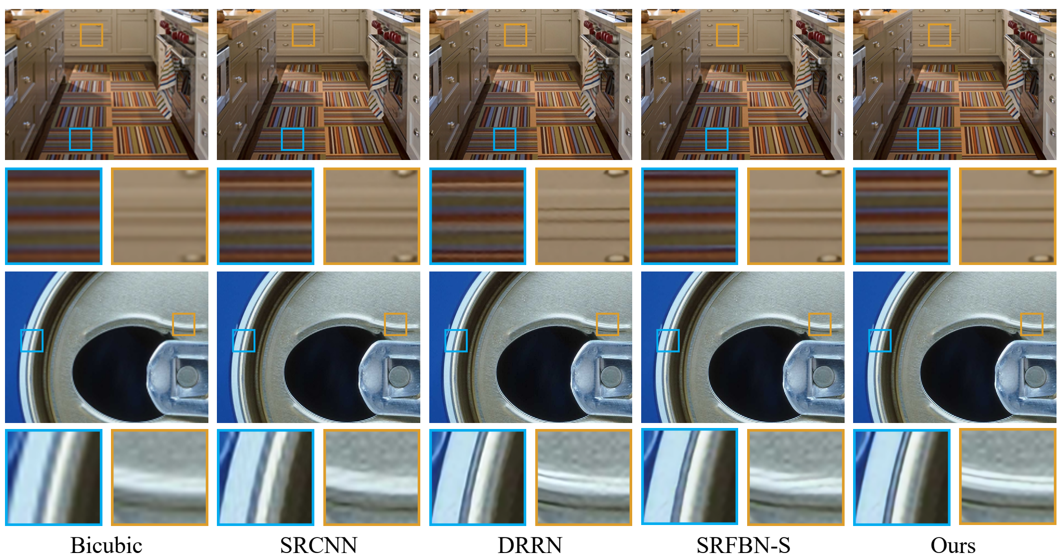

Figure 8: Image super-resolution examples on $\times 4$ scale of general cases in the wild.

Our method has fast inference speed. To obtain a 1280×720 output in the $\times 4$ setting, LAPAR-A, LAPAR-B and LAPAR-C cost 37.3ms, 29.1ms and 22.2ms on a single NVIDIA 2080Ti GPU.

Examples are visualized in Figure 7 and Figure 8. Compared with other methods, LAPAR can generate results with better visual effects. The structures and details are clearly better recovered.

3.5 Image Denoising and JPEG Image Deblocking

In this part, we make further exploration of image denoising and deblocking based on LAPAR.

Image Denoising. Following [40, 58], the noisy images are synthesized. To handle noise with different levels, we train the model with a broad noise standard deviation range (i.e., $\sigma_{noise} \in [0, 55]$). Besides, the upsampling layer of $LaparNet$ in Figure 2 is removed. The predicted filters directly work on the noisy input. We stick to the original filter dictionary and optimize the model parameters in the same manner as the presented SISR task. The denoised results in Figure 9 show that LAPAR removes the blind noise effectively. Compared with other methods [59, 58], LAPAR achieves impressive performance on restoring the original color and structure of the test images.

JPEG Image Deblocking. Besides denoising, LAPAR is also good at JPEG image deblocking. During training, the inputs to the network are JPEG-compressed images with varying quality of $20 \sim 50$. As the testing cases shown in Figure 10, our method removes the JPEG artifacts successfully and obtains superior results compared with DnCNN [58] that is an effective deblocking approach.

GT | (22.49dB, 0.6320) Input | (28.24dB, 0.8843) BM3D | (29.00dB, 0.9025) DnCNN | (**29.80**dB, **0.9161**) Ours

Figure 9: Denoising examples. The values beneath images represent the PSNR(dB) and SSIM. The standard deviation of noise is set to 35.

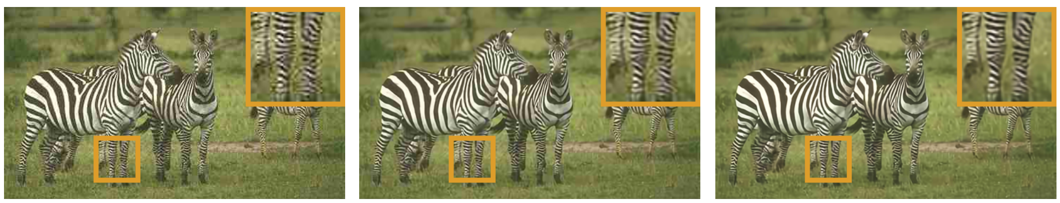

(28.46dB, 0.8459) | (30.42dB, 0.8704) | (**30.87**dB, **0.8733**)

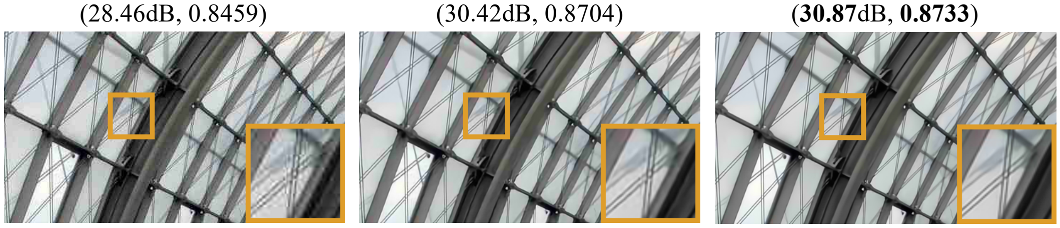

(29.16dB, 0.8706) Input | (31.68dB, 0.9204) DnCNN | (**32.37**dB, **0.9332**) Ours

Figure 10: JPEG image deblocking examples. The values beneath images represent the PSNR(dB) and SSIM. The JPEG quality is set to 20.

4 Conclusion

We have presented a linearly-assembled pixel-adaptive regression network (LAPAR) for image super-resolution. Extensive experiments have demonstrated the effectiveness of the proposed learning strategy. Among lightweight methods, LAPAR achieves state-of-the-art results on multiple benchmarks. Besides, we also show that LAPAR is easily extended to other low-level restoration tasks e.g., denoising and JPEG deblocking, and obtains decent result quality. In future work, we plan to investigate other compact representations of the filter dictionary and joint multi-task optimization.

Broader Impact

This paper aims to promote academic development. In the past decades, image super-resolution, denoising and deblocking techniques have marked new milestones and also been widely used in industry. As far as we know, they have no negative impact on the ethical and societal aspects.

Acknowledgments and Disclosure of Funding

GPUs supported by SmartMore Technology.

References

[1] Jiao Yang, John Wright, Thomas S Huang, and Yi Ma. Image super-resolution via sparse representation. *TIP*, 19(11):2861–2873, 2010.

[2] Roman Zeyde, Michael Elad, and Matan Protter. On single image scale-up using sparse-representations. In *International conference on curves and surfaces*, pages 711–730. Springer, 2010.

[3] Florent Couzinie-Devy, Julien Mairal, Francis Bach, and Jean Ponce. Dictionary learning for deblurring and digital zoom. *arXiv preprint arXiv:1110.0957*, 2011.

[4] Jianchao Yang, Zhaowen Wang, Zhe Lin, Scott Cohen, and Thomas Huang. Coupled dictionary training for image super-resolution. *TIP*, 21(8):3467–3478, 2012.

[5] Yaniv Romano, John Isidoro, and Peyman Milanfar. Raisr: Rapid and accurate image super resolution. *IEEE Transactions on Computational Imaging*, 3(1):110–125, 2016.

[6] Chao Dong, Chen Change Loy, Kaiming He, and Xiaoou Tang. Learning a deep convolutional network for image super-resolution. In *ECCV*, pages 184–199. Springer, 2014.

[7] Jiwon Kim, Jung Kwon Lee, and Kyoung Mu Lee. Accurate image super-resolution using very deep convolutional networks. In *CVPR*, pages 1646–1654, 2016.

[8] Wenzhe Shi, Jose Caballero, Ferenc Huszár, Johannes Totz, Andrew P Aitken, Rob Bishop, Daniel Rueckert, and Zehan Wang. Real-time single image and video super-resolution using an efficient sub-pixel convolutional neural network. In *CVPR*, pages 1874–1883, 2016.

[9] Jiwon Kim, Jung Kwon Lee, and Kyoung Mu Lee. Deeply-recursive convolutional network for image super-resolution. In *CVPR*, pages 1637–1645, 2016.

[10] Wei-Sheng Lai, Jia-Bin Huang, Narendra Ahuja, and Ming-Hsuan Yang. Deep laplacian pyramid networks for fast and accurate super-resolution. In *CVPR*, pages 624–632, 2017.

[11] Ying Tai, Jian Yang, and Xiaoming Liu. Image super-resolution via deep recursive residual network. In *CVPR*, pages 3147–3155, 2017.

[12] Muhammad Haris, Gregory Shakhnarovich, and Norimichi Ukita. Deep back-projection networks for super-resolution. In *CVPR*, pages 1664–1673, 2018.

[13] Yulun Zhang, Kunpeng Li, Kai Li, Lichen Wang, Bineng Zhong, and Yun Fu. Image super-resolution using very deep residual channel attention networks. In *ECCV*, pages 286–301, 2018.

[14] Kai Zhang, Wangmeng Zuo, and Lei Zhang. Learning a single convolutional super-resolution network for multiple degradations. In *CVPR*, pages 3262–3271, 2018.

[15] Tao Dai, Jianrui Cai, Yongbing Zhang, Shu-Tao Xia, and Lei Zhang. Second-order attention network for single image super-resolution. In *CVPR*, pages 11065–11074, 2019.

[16] Zhengxiong Luo, Yan Huang, Shang Li, Liang Wang, and Tieniu Tan. Unfolding the alternating optimization for blind super resolution, 2020.

[17] Steve Bako, Thijs Vogels, Brian McWilliams, Mark Meyer, Jan Novák, Alex Harvill, Pradeep Sen, Tony Derose, and Fabrice Rousselle. Kernel-predicting convolutional networks for denoising monte carlo renderings. *ACM Trans. Graph.*, 36(4):97–1, 2017.

[18] Younghyun Jo, Seoung Wug Oh, Jaeyeon Kang, and Seon Joo Kim. Deep video super-resolution network using dynamic upsampling filters without explicit motion compensation. In *CVPR*, pages 3224–3232, 2018.

[19] Xuecai Hu, Haoyuan Mu, Xiangyu Zhang, Zilei Wang, Tieniu Tan, and Jian Sun. Meta-sr: a magnification-arbitrary network for super-resolution. In *CVPR*, pages 1575–1584, 2019.

[20] Kai Zhang, Luc Van Gool, and Radu Timofte. Deep unfolding network for image super-resolution. *arXiv preprint arXiv:2003.10428*, 2020.

[21] Ben Mildenhall, Jonathan T Barron, Jiawen Chen, Dillon Sharlet, Ren Ng, and Robert Carroll. Burst denoising with kernel prediction networks. In *CVPR*, pages 2502–2510, 2018.

[22] Simon Niklaus, Long Mai, and Feng Liu. Video frame interpolation via adaptive convolution. In *CVPR*, pages 670–679, 2017.

[23] Tianfan Xue, Jiajun Wu, Katherine Bouman, and Bill Freeman. Visual dynamics: Probabilistic future frame synthesis via cross convolutional networks. In *Advances in neural information processing systems*, pages 91–99, 2016.

[24] Xu Jia, Bert De Brabandere, Tinne Tuytelaars, and Luc V Gool. Dynamic filter networks. In *NeurIPS*, pages 667–675, 2016.

[25] Ziwei Liu, Raymond A Yeh, Xiaoou Tang, Yiming Liu, and Aseem Agarwala. Video frame synthesis using deep voxel flow. In *ICCV*, pages 4463–4471, 2017.

[26] Tim Salimans and Durk P Kingma. Weight normalization: A simple reparameterization to accelerate training of deep neural networks. In *NeurIPS*, pages 901–909, 2016.

[27] Marco Bevilacqua, Aline Roumy, Christine Guillemot, and Marie Line Alberi-Morel. Low-complexity single-image super-resolution based on nonnegative neighbor embedding. 2012.

[28] Radu Timofte, Vincent De Smet, and Luc Van Gool. Anchored neighborhood regression for fast example-based super-resolution. In *ICCV*, pages 1920–1927, 2013.

[29] Leonid I Rudin and Stanley Osher. Total variation based image restoration with free local constraints. In *Proceedings of 1st International Conference on Image Processing*, volume 1, pages 31–35. IEEE, 1994.

[30] Antonin Chambolle, Vicent Caselles, Daniel Cremers, Matteo Novaga, and Thomas Pock. An introduction to total variation for image analysis. *Theoretical foundations and numerical methods for sparse recovery*, 9(263-340):227, 2010.

[31] Pietro Perona and Jitendra Malik. Scale-space and edge detection using anisotropic diffusion. *IEEE Transactions on pattern analysis and machine intelligence*, 12(7):629–639, 1990.

[32] Matthew Loper, Naureen Mahmood, Javier Romero, Gerard Pons-Moll, and Michael J Black. Smpl: A skinned multi-person linear model. *TOG*, 34(6):1–16, 2015.

[33] Daniel Zoran and Yair Weiss. From learning models of natural image patches to whole image restoration. In *ICCV*, pages 479–486. IEEE, 2011.

[34] Domen Tabernik, Matej Kristan, Jeremy L Wyatt, and Aleš Leonardis. Towards deep compositional networks. In *ICPR*, pages 3470–3475. IEEE, 2016.

[35] Domen Tabernik, Matej Kristan, and Aleš Leonardis. Spatially-adaptive filter units for deep neural networks. In *CVPR*, pages 9388–9396, 2018.

[36] Bruce Gooch, Erik Reinhard, and Amy Gooch. Human facial illustrations: Creation and psychophysical evaluation. *TOG*, 23(1):27–44, 2004.

[37] Holger Winnemöller, Sven C Olsen, and Bruce Gooch. Real-time video abstraction. *TOG*, 25(3):1221–1226, 2006.

[38] Henry Kang, Seungyong Lee, and Charles K Chui. Coherent line drawing. In *Proceedings of the 5th international symposium on Non-photorealistic animation and rendering*, pages 43–50, 2007.

[39] Jan Eric Kyprianidis and Jürgen Döllner. Image abstraction by structure adaptive filtering. In *TPCG*, pages 51–58, 2008.

[40] Pascal Getreuer, Ignacio Garcia-Dorado, John Isidoro, Sungjoon Choi, Frank Ong, and Peyman Milanfar. Blade: Filter learning for general purpose computational photography. In *ICCP*, pages 1–11. IEEE, 2018.

[41] Chaofeng Wang, Zheng Li, and Jun Shi. Lightweight image super-resolution with adaptive weighted learning network. *arXiv preprint arXiv:1904.02358*, 2019.

[42] Eirikur Agustsson and Radu Timofte. Ntire 2017 challenge on single image super-resolution: Dataset and study. In *CVPRW*, pages 126–135, 2017.

[43] Zhou Wang, Alan C Bovik, Hamid R Sheikh, and Eero P Simoncelli. Image quality assessment: from error visibility to structural similarity. *TIP*, 13(4):600–612, 2004.

[44] David Martin, Charless Fowlkes, Doron Tal, and Jitendra Malik. A database of human segmented natural images and its application to evaluating segmentation algorithms and measuring ecological statistics. In *ICCV*, volume 2, pages 416–423. IEEE, 2001.

[45] Jia-Bin Huang, Abhishek Singh, and Narendra Ahuja. Single image super-resolution from transformed self-exemplars. In *Proceedings of the IEEE conference on computer vision and pattern recognition*, pages 5197–5206, 2015.

[46] Yusuke Matsui, Kota Ito, Yuji Aramaki, Azuma Fujimoto, Toru Ogawa, Toshihiko Yamasaki, and Kiyoharu Aizawa. Sketch-based manga retrieval using manga109 dataset. *Multimedia Tools and Applications*, 76(20):21811–21838, 2017.

[47] Zhen Li, Jinglei Yang, Zheng Liu, Xiaomin Yang, Gwanggil Jeon, and Wei Wu. Feedback network for image super-resolution. In *CVPR*, pages 3867–3876, 2019.

[48] Namhyuk Ahn, Byungkon Kang, and Kyung-Ah Sohn. Fast, accurate, and lightweight super-resolution with cascading residual network. In *ECCV*, pages 252–268, 2018.

[49] Bee Lim, Sanghyun Son, Heewon Kim, Seungjun Nah, and Kyoung Mu Lee. Enhanced deep residual networks for single image super-resolution. In *CVPR Workshops*, July 2017.

[50] Yulun Zhang, Kunpeng Li, Kai Li, Lichen Wang, Bineng Zhong, and Yun Fu. Image super-resolution using very deep residual channel attention networks. In *ECCV*, 2018.

[51] Xintao Wang, Ke Yu, Shixiang Wu, Jinjin Gu, Yihao Liu, Chao Dong, Yu Qiao, and Chen Change Loy. Esrgan: Enhanced super-resolution generative adversarial networks. In *ECCV Workshops*, September 2018.

[52] W. Yifan, F. Perazzi, B. McWilliams, A. Sorkine-Hornung, O Sorkine-Hornung, and C. Schroers. A fully progressive approach to single-image super-resolution. In *CVPR Workshops*, June 2018.

[53] Chao Dong, Chen Change Loy, and Xiaoou Tang. Accelerating the super-resolution convolutional neural network. In *ECCV*, pages 391–407. Springer, 2016.

[54] Ying Tai, Jian Yang, Xiaoming Liu, and Chunyan Xu. Memnet: A persistent memory network for image restoration. In *ICCV*, pages 4539–4547, 2017.

[55] Jae-Seok Choi and Munchurl Kim. A deep convolutional neural network with selection units for super-resolution. In *CVPRW*, pages 154–160, 2017.

[56] Xiangxiang Chu, Bo Zhang, Hailong Ma, Ruijun Xu, Jixiang Li, and Qingyuan Li. Fast, accurate and lightweight super-resolution with neural architecture search. *arXiv preprint arXiv:1901.07261*, 2019.

[57] Tong Tong, Gen Li, Xiejie Liu, and Qinquan Gao. Image super-resolution using dense skip connections. In *ICCV*, pages 4799–4807, 2017.

[58] Kai Zhang, Wangmeng Zuo, Yunjin Chen, Deyu Meng, and Lei Zhang. Beyond a gaussian denoiser: Residual learning of deep cnn for image denoising. *TIP*, 26(7):3142–3155, 2017.

[59] Kostadin Dabov, Alessandro Foi, Vladimir Katkovnik, and Karen Egiazarian. Image denoising by sparse 3-d transform-domain collaborative filtering. *TIP*, 16(8):2080–2095, 2007.